LASER INTERFEROMETER GRAVITATIONAL WAVE OBSERVATORY
- LIGO -
CALIFORNIA INSTITUTE OF TECHNOLOGY
MASSACHUSETTS INSTITUTE OF TECHNOLOGY

Technical Note	**LIGO-T22xxxxx–**	2023/09/21

Sensor Fusion for Improved Length Sensing and Control: Final Report

Deven Bowman

California Institute of Technology
LIGO Project, MS 18-34
Pasadena, CA 91125
Phone (626) 395-2129
Fax (626) 304-9834
E-mail: info@ligo.caltech.edu

Massachusetts Institute of Technology
LIGO Project, Room NW22-295
Cambridge, MA 02139
Phone (617) 253-4824
Fax (617) 253-7014
E-mail: info@ligo.mit.edu

LIGO Hanford Observatory
Route 10, Mile Marker 2
Richland, WA 99352
Phone (509) 372-8106
Fax (509) 372-8137
E-mail: info@ligo.caltech.edu

LIGO Livingston Observatory
19100 LIGO Lane
Livingston, LA 70754
Phone (225) 686-3100
Fax (225) 686-7189
E-mail: info@ligo.caltech.edu

http://www.ligo.caltech.edu/

Contents

1 Introduction

Gravitational waves are distortions in spacetime produced by accelerating masses. Their existence was predicted over 100 years ago with the development of general relativity and the first experimental observation was made on September 14, 2015 by the Laser Interferometer Gravitational Wave Observatory (LIGO) and Virgo collaborations of gravitational waves produced by a merger of 2 black holes.[1].

The Advanced LIGO detector is a pair of Michelson interferometers in Washington State and Louisiana with 4km arms [4]. The detector design includes several optical cavities to increase sensitivity. These include Faby-Perot cavities in each arm, a power recycling cavity, and a signal recycling cavity. A diagram is shown on the left of figure 1.

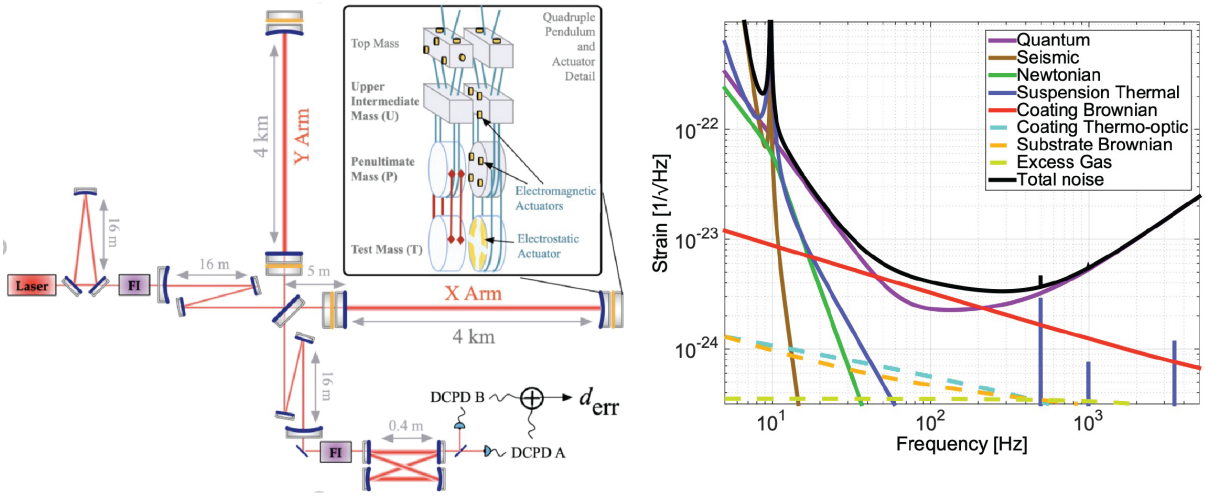

Figure 1: On the left, a diagram of one of the Advanced LIGO detectors [2]. On the right, the sensitivity curve of Advanced LIGO [3]. Each line shows the amplitude spectral density of a noise source. The total combination, in black, produces the predicted noise floor for advanced LIGO.

Gravitational waves cause the arms of the interferometer to lengthen and contract relative to each other as the wave propagates through the detector. This changes the path length for light traveling in each arm, producing a relative phase difference detectable through interference. The fractional change in the length of the arms of the detector is known as strain and is proportional to the amplitude of the gravitational wave signal. Advanced LIGO's strain sensitivity curve is shown on the right of figure 1. The black curve, which is a combination of the individual noise sources shown in other colors, represents the minimum amplitude gravitational wave signal detectable in each frequency band.

There are many length degrees of freedom (DoF) that must be controlled for the detector to operate. Figure 2 shows these degrees of freedoms and the sensors used to generate error signals. The most important of these is DARM, defined below.

$$L_{-} = \frac{L_x - L_y}{2} \tag{1}$$

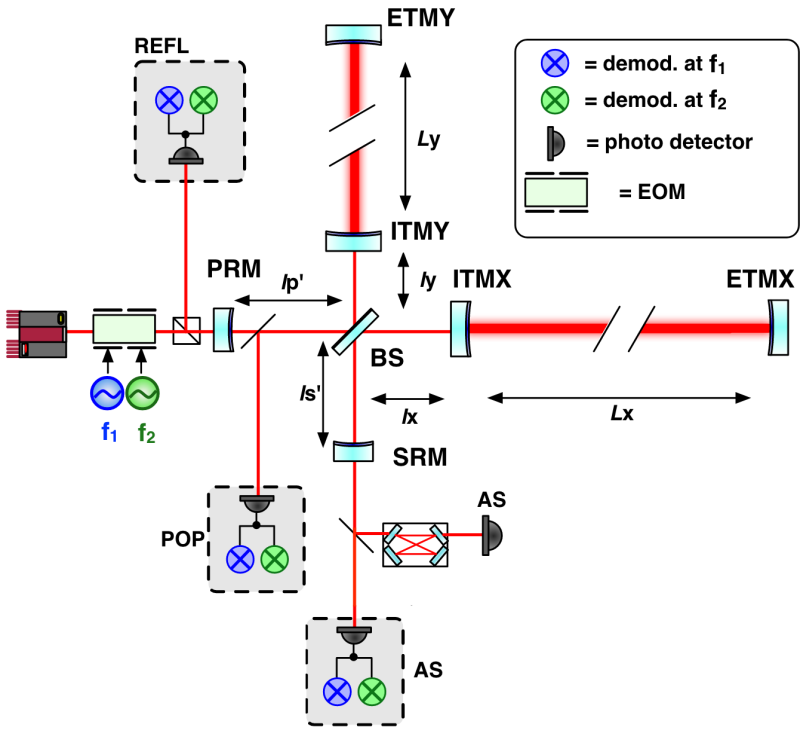

Figure 2: A diagram of one of the Advanced LIGO detectors [5]. REFL, POP, and AS denote collections of photodiodes measuring at DC and radio frequencies (RFPDS).

For the detector to operate, these length DoFs need to be controlled. This is achieved by deriving error signals from sensors around the detector. These error signals drive feedback loops that keep the detector at its operating point. A block diagram of a simplified control loop for DARM is shown in figure 3. The plant of the control system is the suspension of the mirrors. These are disturbed by the gravitational wave signal and noise causing additional displacement to the mirrors. The sensors converts this to an error signal for DARM and the control block uses the error signal to drive actuators that apply force to the mirrors to return them to the set point. The DARM error signal can be calculated from the open loop transfer functions.

$$DARM = \frac{S}{1 - SPC}(n + g_w) \tag{2}$$

This length control system is needed to stabilize the detector against displacement noise to maintain a linear response to fluctuations in its DoF. However, by controlling mirror motion against displacements, the mirror motion due to gravitational wave signals is also suppressed. The gravitational wave signal is attained by applying the inverse of the closed loop transfer function from the error signal to DARM.

$$g_w = \frac{1 - \hat{S}\hat{P}\hat{C}}{\hat{S}} DARM \tag{3}$$

The hats on the inverse transfer functions indicate that they are models that must be measured for accurate readout of the signal.

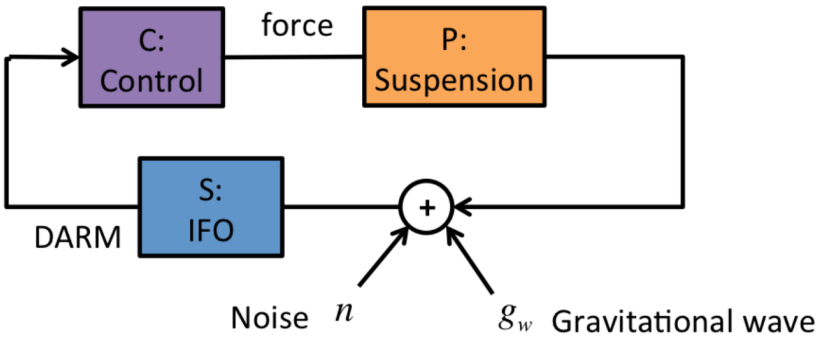

Figure 3: The control loop for DARM shown with the injection of displacement noise and gravitational wave signal [6].

The control system is a key part of the detectors function. Currently, there are more sensors with some coupling to the length DoFs than there are length DoFs. A linear system that uses the outputs of all of these sensors would be overdetermined. The current control techniques only employ a subset of the sensors to generate a determined system: equal numbers of DoFs and sensors. This project will explore the potential benefits to the sensitivity of the detector from designing an overdetermined control system that can take advantage of noise correlations between the sensors to reduce the susceptibility of the control system to various noise inputs.

2 PRMI Configuration

We consider the simplified detector configuration of a Michelson interferometer with a power recycling cavity(PRMI). This is a simplification of the Advanced LIGO detector configuration since there are no Fabry-Perot cavities in the detector arms and no signal recycling mirror after the anti-symmetric port of the beam splitter to form a signal recycling cavity. There are two important length DoFs in this configuration, MICH and PRCL, defined in equations 4 and 5 respectively based on length definitions in figure 2. MICH is the difference in the arm lengths and PRCL is the length of the power recycling cavity.

$$l_- = \frac{l_x - l_y}{2} \tag{4}$$

$$l_p = l'_p + \frac{l_x + l_y}{2} \tag{5}$$

The 40m LIGO prototype at the California Institute of Technology is a 1:100 scale version of the Advanced LIGO detectors. This instrument is used for research and development of technologies for future gravitational wave detectors. This project will study the PRMI configuration of the 40m prototype.

3 40m LIGO prototype PRMI Length Control System

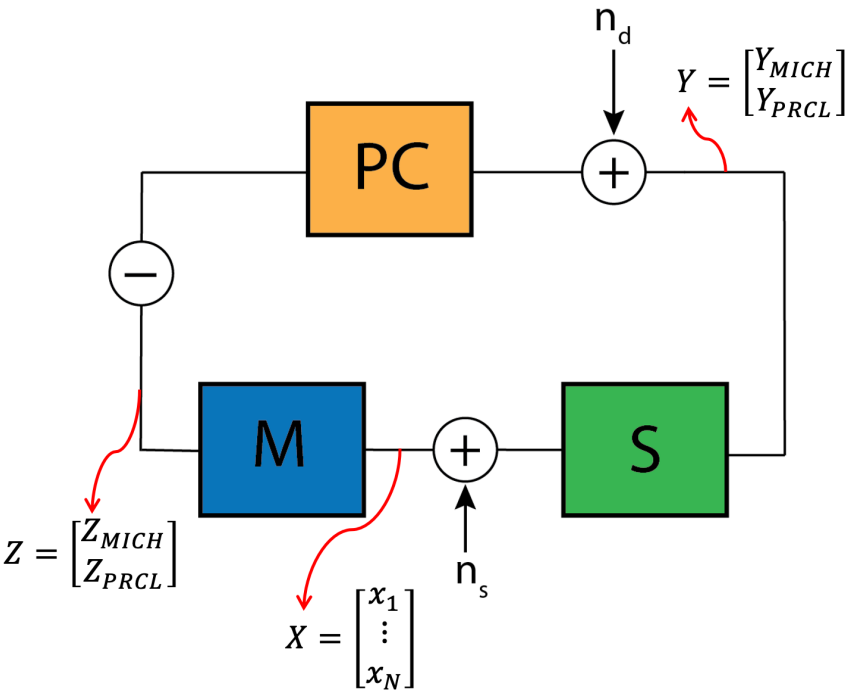

Figure 4: The block diagram for the control loop for MICH and PRCL in the PRMI configuration is shown.

A block diagram representing the relevant structure of the control system for MICH and PRCL is shown in figure 4. **PC** is the transfer function containing the control filters and the mechanical plant. Y measures the fluctuations in MICH and PRCL from their set point. In symbols, we can take the differential of both sides of equations 4 and 5 to get equations 6.

$$Y = \begin{bmatrix} \delta l_- \\ \delta l_p \end{bmatrix} = \begin{bmatrix} \frac{\delta l_x - \delta l_y}{2} \\ \delta l'_p + \frac{\delta l_x + \delta l_y}{2} \end{bmatrix} \tag{6}$$

S is the Nx2 sensing matrix that maps MICH and PRCL states to the values measured by the N different sensors which are stored in X. **M** is the 2xN sensor fusion matrix which linearly combines the N sensors into 2 fused sensors, Z. Displacement noise, n_d, causes fluctuations in MICH and PRCL that need to be suppressed by controls. Sensing noise, n_s, represents all other noises that enter the loop due to the sensing and control process. This includes laser noise, ADC noise, photodiode dark noise, and other sources which can be correlated or uncorrelated between the detectors. The feedback system causes n_s to propagate to Y and become additional noise on MICH and PRCL. This is why care must be taken to generate the error signals for control. The current design of **M** selects one sensor for each DoF to generate an error signal and discards the rest of the sensors. Currently, PRCL is sensed with a REFL photodiode demodulated at 11MHz and MICH is sensed by an AS photodiode demodulated at 55 MHz.

Table 1: A subset of the RFPDs used for the initial study of the PRMI LSC system are tabulated

Type	Demod frequency (MHz)	Demod phase (degrees)
AS	55	in-phase
AS	55	quadrature
REFL	55	in-phase
REFL	55	quadrature
REFL	11	in-phase
REFL	11	quadrature
REFL	165	in-phase
REFL	165	quadrature

4 PRMI LSC measurements

The 40m LIGO prototype was locked in the PRMI configuration by several of the LIGO lab staff. This allowed for open loop transfer functions for the MICH and PRCL control loops to be measured. These are shown in figure 5. 80 seconds of data was taken from 8 RF photodiodes, listed in table 1.

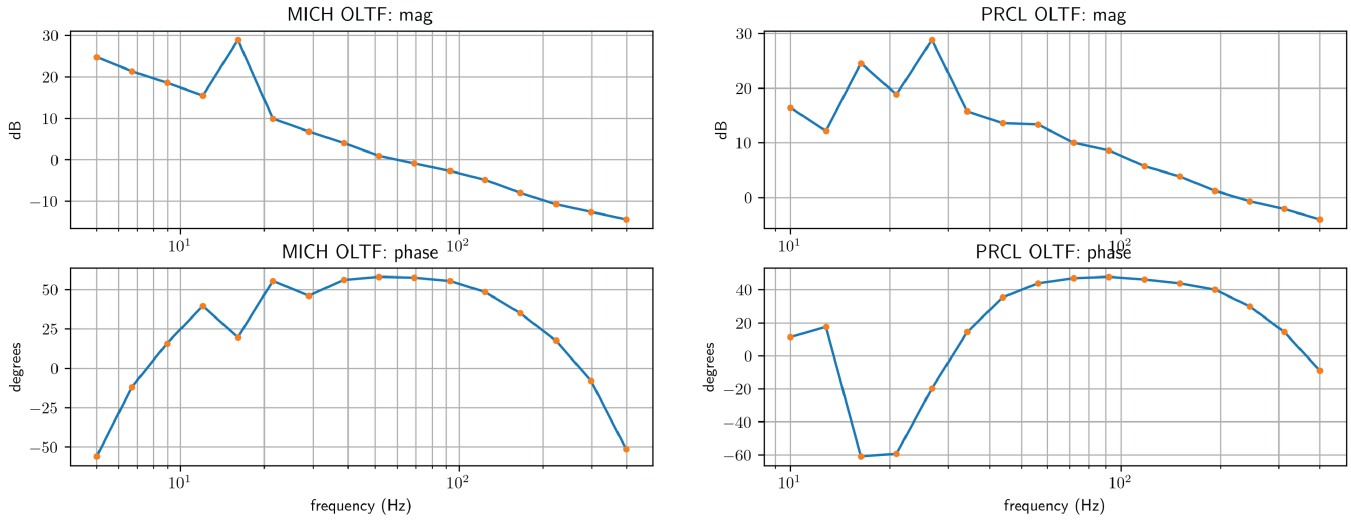

Figure 5: The measured open loop transfer functions for MICH and PRCL during the PRMI lock are shown. The coherence of the measured PRCL OLTF was poor below 60 Hz so the gain and phase were extrapolated from higher frequencies for use in calculations.

The amplitude spectral densities(ASD) of the sensor signals are shown in 6. These signals will be calibrated into meters for multiple choices of **M** in later plots.

Table 2: The response of each detector to MICH and PRCL are shown. These elements form the sensing matrix.

Sensors	MICH (counts/meter)	PRCL (counts/meter)
AS55-I	$(+4.44 \pm 2.93)e+08$	$(+1.69 \pm 0.37)e+10$
AS55-Q	$(+9.89 \pm 1.00)e+09$	$(-3.77 \pm 0.50)e+09$
REFL11-I	$(-1.43 \pm 0.53)e+10$	$(+9.13 \pm 0.86)e+11$
REFL11-Q	$(-7.73 \pm 3.71)e+08$	$(+5.13 \pm 0.50)e+10$
REFL55-I	$(-6.12 \pm 2.24)e+11$	$(+3.70 \pm 0.37)e+13$
REFL55-Q	$(+1.46 \pm 0.53)e+11$	$(-8.89 \pm 0.86)e+12$
REFL165-I	$(-3.73 \pm 0.49)e+09$	$(+6.20 \pm 0.60)e+10$
REFL165-Q	$(-1.38 \pm 0.10)e+09$	$(-2.24 \pm 0.17)e+10$

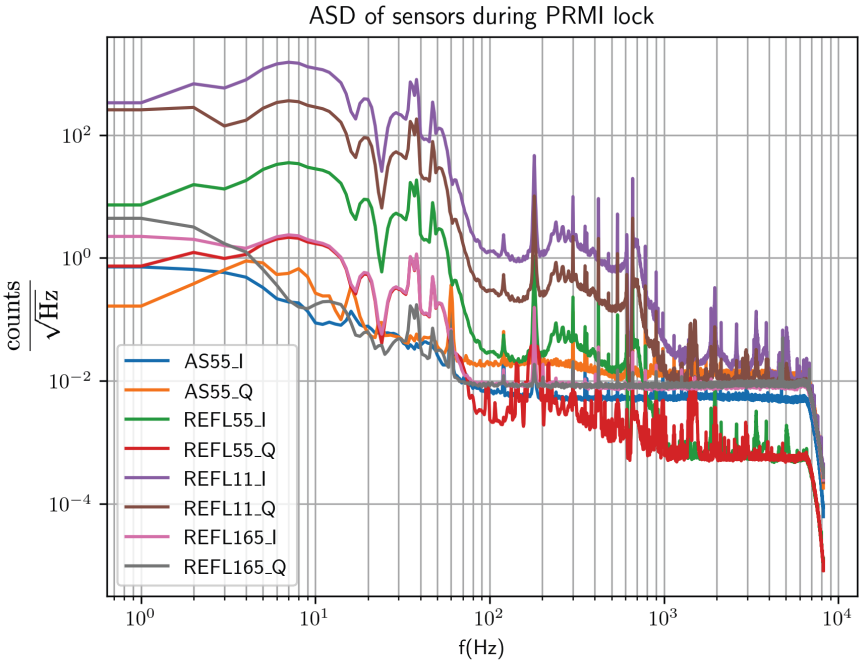

Figure 6: The amplitude spectral density of the uncalibrated sensors signals during the PRMI lock are shown.

The sensing matrix was measured by driving MICH and PRCL with sinusoids at 211.1 Hz and 313.31 Hz respectively. The results are shown in table 2.

5 Data Analysis

In this section, I'll develop the mathematical framework needed to simulate the performance of the PRMI control loop with an arbitrary choice of sensor fusion.

5.1 Relevant Transfer Functions

The block diagram in figure 4 tells us how the various signals can be related mathematically. The sensor signals,X, can be calculated in terms of the injected noises.

$$X = (\mathbf{I} + \mathbf{SPCM}_0)^{-1} (\mathbf{S}n_d + n_s) \tag{7}$$

$$\mathbf{M}_0 = \begin{bmatrix} 0 & 1 & 0 & 0 & 0 & 0 & 0 & 0 \\ 0 & 0 & 1 & 0 & 0 & 0 & 0 & 0 \end{bmatrix} \tag{8}$$

$\mathbf{M}_0$ is the fusion matrix used during the PRMI lock that selects the AS55 quadrature-phase sensor for MICH and the REFL11 in-phase sensor for PRCL. The unsuppressed noises can be calculated from the sensor signals by transforming with $(\mathbf{I} + \mathbf{SPCM}_0.)$. The unsuppressed noise can be defined as follows.

$$\tilde{X} = (\mathbf{I} + \mathbf{SPCM}_0) X \tag{9}$$

Then, the closed loop suppression of the feedback system with an alternative $\mathbf{M}$ can be calculated by mapping with $(\mathbf{I} + \mathbf{SPCM}.)^{-1}$. The simulated sensor signals, X_{sim}, are defined as follows.

$$X_{sim} = (\mathbf{I} + \mathbf{SPCM})^{-1} \tilde{X} = (\mathbf{I} + \mathbf{SPCM})^{-1} (\mathbf{I} + \mathbf{SPCM}_0) X \tag{10}$$

The signal in the fused sensors can be calculated by mapping X_{sim} by $\mathbf{M}$.

$$Z_{sim} = \mathbf{M}X_{sim} = \mathbf{M} (\mathbf{I} + \mathbf{SPCM})^{-1} (\mathbf{I} + \mathbf{SPCM}_0) X \tag{11}$$

Finally, the simulated noises that would be measured on MICH and PRCL given $\mathbf{M}$ can be calculated from transforming Z_{sim} by $(\mathbf{MS})^{-1}$.

$$Y_{sim} = (\mathbf{MS})^{-1} Z_{sim} = (\mathbf{MS})^{-1} \mathbf{M} (\mathbf{I} + \mathbf{SPCM})^{-1} (\mathbf{I} + \mathbf{SPCM}_0) X \tag{12}$$

$\mathbf{M}$ and $\mathbf{S}$ are rectangular matrices so they do not have unique inverses, but their product, $\mathbf{MS}$, is a 2x2 matrix with a unique inverse that determines how the fused sensors relate to MICH and PRCL . An important consequence of this is that the $(\mathbf{MS})^{-1}\mathbf{M}$ factor in equation 12 does not simplify to cancel $\mathbf{M}$. We'll denote the complete transfer function from X to Y_{sim} as $\mathbf{G}_{X,Y_{sim}}$.

5.2 Power Spectral Densities of Frequency Domain Transformed Signals

The power spectral densities of the new signals derived from frequency domain transformation of the measured signals, X, are important for understanding performance of the sensor fusion matrices.

Suppose we have two frequency domain signal vectors $V(\omega)$ and $W(\omega)$ related by a transfer function $\mathbf{A}$, with elements $a(\omega)_{ij}$. The ith signal in V is the following.

$$v_i(\omega) = \Sigma_j^N a(\omega)_{ij} w(\omega)_j \tag{13}$$

The cross spectral density between $v(\omega)_k$ and $v(\omega)_l$ can be calculated as follows.

$$CSD(v_k, v_l) = \lim_{T\to\infty} \frac{1}{T} v_k^* v_l = \lim_{T\to\infty} \frac{1}{T} \Sigma_i^N \Sigma_j^N (a(\omega)_{ki} w(\omega)_i)^* a(\omega)_{lj} w(\omega)_j \tag{14}$$

T is the time over which the signal is observed. We can move the sum and the factors $a(\omega)_{ki}^* a(\omega)_{lj}$ outside the limit since they have no dependence on T and we can assume that $CSD(x_i, x_j)$ is well defined for all i, j.

$$CSD(v_k, v_l) = \Sigma_i^N \Sigma_j^N a(\omega)_{ki}^* a(\omega)_{lj} \lim_{T\to\infty} \frac{1}{T} w(\omega)_i^* w(\omega)_j = \Sigma_i^N \Sigma_j^N a(\omega)_{ki}^* a(\omega)_{lj} CSD(w_i, w_j) \tag{15}$$

We can rewrite this last expression in a more concise form.

$$CSD(v_k, v_l) = \mathbf{A}_k \mathbf{CSD}(W) \mathbf{A}_l^H \tag{16}$$

$\mathbf{CSD}(W)$ refers to a matrix where the i, j element is $CSD(w_i, w_j)$ and $\mathbf{A}_i$ is column i of the transfer function matrix $\mathbf{A}$ and superscript H denotes hermitian conjugate. It follows that $\mathbf{CSD}(V)$ permits a simple expression in terms of $\mathbf{CSD}(W)$.

$$\mathbf{CSD}(V) = \mathbf{A}\mathbf{CSD}(W)\mathbf{A}^H \tag{17}$$

Therefore we can use the transfer functions calculated in the last section to transform $\mathbf{CSD}(X)$, the matrix of cross spectral densities of the sensors measured in the PRMI lock, to calculate the cross spectral density of the signals in the simulated control system. The main use of this is to calculate the simulated amplitude spectral densities of MICH and PRCL with sensor fusion. This is done in equation 18 that uses the $\mathbf{G}_{X,Y_{sim}}$ transfer function calculated in the previous section. The MICH and PRCL ASDs are the square root of the diagonal terms of $\mathbf{CSD}(Y_{sim})$.

$$\mathbf{CSD}(Y_{sim}) = \mathbf{G}_{X,Y_{sim}} \mathbf{CSD}(X) \mathbf{G}_{X,Y_{sim}}^H \tag{18}$$

6 Proposed Sensor Fusion Matrices and Simulated Results

In this section, I will describe the methods for sensor fusion that I investigated and use the calculations above to simulate their performance for the PRMI control loop.

6.1 Diagonalization of MS

The product matrix **MS** maps from the MICH and PRCL signals to the virtual sensors. Therefore, it is natural to consider choices of **M** that diagonalize **MS**. The current choice of sensor fusion matrix does not diagonalize **MS**.

$$\mathbf{M_0 S} = \begin{bmatrix} 9.89e+09 & -3.77e+09 \\ -1.43e+10 & 9.13e+11 \end{bmatrix} \tag{19}$$

The large off diagonal components result in cross coupling between MICH and PRCL. Therefore a simple potential improvement will be to choose the new sensor fusion matrix to diagonalize **MS** and maintain the same on diagonal components.

$$\mathbf{MS} = \begin{bmatrix} 9.89e+09 & 0 \\ 0 & 9.13e+11 \end{bmatrix} \tag{20}$$

One choice for **M** that satisfies this condition uses the Moore-Penrose inverse of **S**, $\mathbf{S}^+$, shown in equation 21. This sensor fusion matrix will be referred to as the Moore-Penrose or MP matrix.

$$\mathbf{M} = \begin{bmatrix} 9.89e+09 & 0 \\ 0 & 9.13e+11 \end{bmatrix} \mathbf{S}^+ \tag{21}$$

Since there are more sensors than DoFs, this condition does not uniquely specify **M**. A further improvement may be attained by specifying a cost function to optimize. This approach was taken to reduce the sensing noise entering the system at high frequencies.

6.2 High Frequency Sensing Noise Optimization

Above a kilohertz, the amplitude spectral densities of the sensor signals are white, reflecting that the signal composition is essentially only sensing noise, as shown by figure 7.

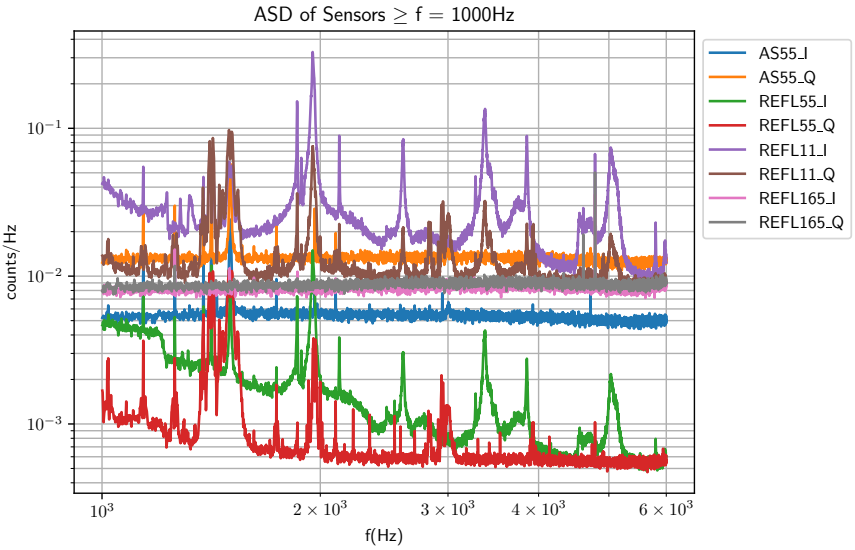

Figure 7: The ASD of the sensor data above 1KHz.

Therefore, $\mathbf{CSD}(\tilde{X})$ is a good approximation of the sensing noise injected into the system at high frequencies. This sensing noise enters the fused sensors, and the rest of the system, through $\mathbf{M}$. Thus the cost function was derived from mapping $\mathbf{CSD}(\tilde{X})$ with $\mathbf{M}$. and then integrating over frequencies (1,6)KHz. The upper bound was chosen to avoid the high frequency cutoff where the ASD in each sensor vanishes.

$$\mathbf{COST} = \int_{1KHz}^{6KHz} \mathbf{CSD}(Z_{n_s}) = \int_{1KHz}^{6KHz} \mathbf{MCSD}(\tilde{X})\mathbf{M}^T \tag{22}$$

Each row of $\mathbf{M}$ defines the sensor fusion for one of the virtual sensors and so they can be optimized independently in this case. Thus the cost functions used to optimize the first row and second rows of $\mathbf{M}$ are the $\mathbf{COST}_{1,1}$ and $\mathbf{COST}_{2,2}$. These optimizations were done with respect to the constraint that $\mathbf{M}$ diagonalize $\mathbf{MS}$ as described. This constraint maintains the amplitude of the signal in each fused sensor. Thus, minimized these cost functions maximizes the high frequency SNR of the fused sensors. The optimization was implemented with `scipy.optimize.minimze()`.

6.3 Sensor Fusion Results

The simulated amplitude spectral densities of MICH and PRCL are shown in figure 8.

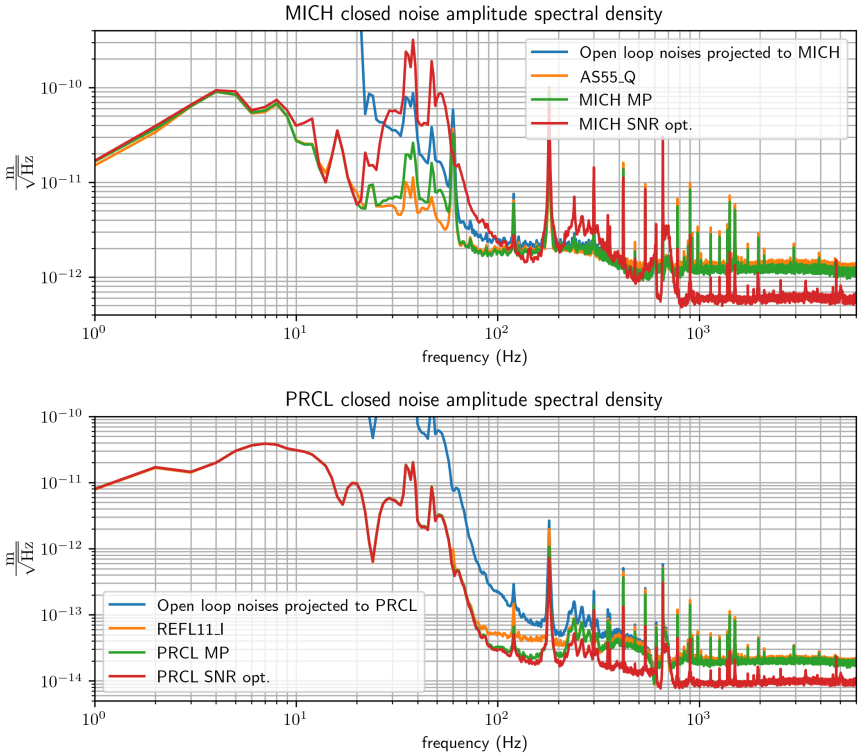

Figure 8: The ASD of the simulated noises on MICH and PRCL for several choices of $\mathbf{M}$.

The open loop noises on MICH and PRCL were calculated by mapping $\mathbf{CSD}(\tilde{X})$ by $\mathbf{S}^+$, the Moore-Penrose inverse of the sensing matrix. The data for the current sensor fusion matrix

is shown in orange, the **M** calculated with the rescaled Moore-Penrose inverse of the sensing matrix is presented in orange, and the results of the high frequency SNR optimized sensor fusion matrix is is shown in red.

At low frequencies the all sensors perform similarly since the MICH and PRCL motion dominates over other noise sources and all the sensors were designed to have the same gain to these signals. This is enforced by the on-diagonal components of the diagonal condition for **MS**. At high frequencies the SNR optimized sensors result in about half the noise in our sensing of MICH and PRCL. For MICH, the SNR optimized sensor has significantly worse performance around 30Hz. This is likely due to noise from PRCL that has coupled into the MICH sensor. The imperfect knowledge of the sensing matrix makes it impossible to eliminate all cross couplings between the two DoFs and the PRCL signal is dominant in all the sensors except `AS55_Q`. Thus, it is particularly challenging to design a MICH sensor with multiple sensors that stays orthogonal to PRCL.

7 Studying Noise Correlations in Calibrated Data

In addition to explicit design of virtual sensors, techniques to learn about noise sources in the data from their frequency dependent correlations between the sensors was studied in this project. With uncalibrated sensor data the relative magnitudes of the sensor signals are undefined. Therefore, the sensors were calibrated to PRCL by rescaling each sensor's signal by the sensing matrix element mapping to that sensor from PRCL. The result is that noise correlations were studied in the context of designing a PRCL virtual sensor. A similar analysis could be done with a MICH calibration but PRCL was chosen since it is the dominant signal at low frequencies in most of the sensors. This calibration was applied directly to $CSD(\tilde{X})$ to calculate the unsuppressed cross spectral density matrix calibrated to PRCL with equation 23.

$$CSD(\tilde{Y}_{PRCL})_{i,j} = \frac{CSD(\tilde{X})_{i,j}}{S_{i,2}S_{j,2}} \tag{23}$$

A tool for analysis of calibrated data was the band-limited covariance matrix. For N sensors, this is an NxN matrix that quantifies the magnitude of the correlated fluctuations between all possible sensor pairs within a specific frequency range. This was employed since many of the noise sources in the sensors, including the displacement noise that we want to sense, are expected to be frequency dependent. The band limited covariance matrix was defined such that integration over the entire frequency range, $(0, \infty)$, would yield the traditional covariance matrix, defined in equation 24 for ergodic zero mean variables.

$$[R_{xx}]_{i,j} = E\{x_i x_j\} = \lim_{T\to\infty} \int_0^T x_i(t)x_j(t)df \tag{24}$$

T is the time over which the variables are measured. The connection to cross spectral densities becomes clear by considering the power spectral density of $x_i + x_j$. By Parseval's Theorem we know that the integral of the power spectral density over all frequencies is equal

to the variance.

$$E\{(x_i + x_j)^2\} = \lim_{T\to\infty} \int_0^\infty PSD(x_i + x_j)df \tag{25}$$

We can expand both sides to see the connections between the cross terms. The left hand side can be rewritten in equation 26 using linearity of expectation values.

$$E\{(x_i + x_j)^2\} = E\{x_i^2\} + E\{x_j^2\} + 2E\{x_i x_j\} \tag{26}$$

The right hand side can be rewritten using cross spectral densities.

$$\int_0^\infty PSD(x_i + x_j)df = \int_0^\infty \left(PSD(x_i) + PSD(x_j) + CSD(x_i, x_i) + CSD(x_j, x_i)\right) df \tag{27}$$

With application of Parseval's Theorem again, we can state the equality of the cross terms.

$$E\{x_i x_j\} = \lim_{T\to\infty} \frac{1}{2} \int_0^\infty \left(CSD(x_i, x_j) + CSD(x_j, x_i)\right) df \tag{28}$$

Therefore the equation 29 was used to defined the band-limited covariance matrix for the frequency range (f_1, f_2).

$$R_{\tilde{y}y}^{f_1,f_2} = \int_{f_1}^{f_2} \frac{1}{2} \left(CSD(\tilde{Y}_{PRCL}) + CSD(\tilde{Y}_{PRCL})^T\right) df \tag{29}$$

Specifically, this is the band-limited covariance of the unsuppressed and PRCL calibrated sensors signals.

7.1 Principal Component Analysis for Noise Peaks

The amplitude spectral density of the calibrated sensor data contains many features that dominate over a particular frequency range. For each of these features, we can model them as an individual noise source, n, which is coupled into the sensors through an Nx1 matrix $\mathbf{S_n}$. This analysis will consider a principal component analysis within the frequency band (f_1, f_2) where a noise peak is dominant.

Within (f_1, f_2), this cross spectral density of $\mathbf{CSD}(\tilde{X})$ is dominated by n.

$$\mathbf{CSD}(\tilde{X}) \approx \mathbf{S_n} PSD(n) \mathbf{S_n}^T \tag{30}$$

After calibration to PRCL this becomes equation 31.

$$\mathbf{CSD}(\tilde{Y}_{PRCL})_{i,j} \approx \frac{(\mathbf{S_n})_i}{\mathbf{S}_{i,2}} PSD(n) \frac{(\mathbf{S_n})_j}{\mathbf{S}_{j,2}} = \mathbf{S}_n^{PRCL} PSD(n) (\mathbf{S}_n^{PRCL})^T \tag{31}$$

I have defined $\mathbf{S}_n^{PRLC}$ to be the to be the PRCL calibrated $\mathbf{S}_n$ matrix. Since $\mathbf{CSD}(\tilde{Y}_{PRCL})$ is symmetric and $\mathbf{S}_n$ is assumed to be frequency independent, the band-limited covariance matrix over this frequency range will be well approximated by the equation 32.

$$\mathbf{R}_{\tilde{y}y}^{f_1,f_2} = \mathbf{S}_n^{PRCL} \int_{f_1}^{f_2} PSD(n)df (\mathbf{S}_n^{PRCL})^T = \mathbf{S}_n^{PRCL} \sigma_n^2 (\mathbf{S}_n^{PRCL})^T = \sigma_n^2 \mathbf{S}_n^{PRCL} (\mathbf{S}_n^{PRCL})^T \tag{32}$$

The last step in equation 32 uses the fact that σ_n^2 is a scalar since we are assuming only one noise source is relevant in this frequency range. Thus, the order of the terms can be rearranged so that the band-limited covariance matrix becomes the outer product of $\mathbf{S}_n^{PRCL}$ scaled by the noise power, σ_n^2, within the frequency range. A singular value decomposition of $\mathbf{S}_n^{PRCL}$ yields equation 33.

$$\mathbf{S}_n^{PRCL} = \mathbf{U}\mathbf{\Sigma}\mathbf{V}^T = \pm\mathbf{U}\mathbf{\Sigma} \tag{33}$$

The first form of the SVD in equation 33 uses the traditional notation where $\mathbf{U}$ is a NxN unitary matrix, $\mathbf{\Sigma}$ is a Nx1 rectangular diagonal matrix, and $\mathbf{V}^T$ is a 1x1 unitary matrix. This is simplified into the last equality in equation 33 since $\mathbf{V}^T$ will be ± 1. The band-limited covariance can be rewritten in diagonalized form in equation 34

$$\mathbf{R}_{\tilde{y}\tilde{y}}^{f_1,f_2} = \mathbf{U}\mathbf{\Sigma}\sigma_n^2\mathbf{\Sigma}^T\mathbf{U}^T \tag{34}$$

The result is that we expect the first principal component of a PCA over this frequency range will be proportional to $\mathbf{S}_n^{PRCL}$. The other N-1 principal components will form an orthonormal basis of the subspace perpendicular to $\mathbf{S}_n^{PRCL}$. Even though the principal components are normalized to 1, they do not remain calibrated to PRCL. This can be achieved by renormalizing them by the sum of their components.

In conclusion, a band-limited PCA may provide information on how dominant noise sources are coupling into the sensors.

7.2 Principal Component Analysis of simulated noise spike

This technique was first evaluated by injecting an artificial noise signal into $\mathbf{CSD}(\tilde{Y}_{PRCL})$. This was done by choosing an $\mathbf{S_n}$ and defining the injected noise cross spectral density matrix, $\mathbf{CSD}(\tilde{\mathbf{Y}}_\mathbf{n})$, to have the form of equation 35.

$$\mathbf{CSD}(\tilde{\mathbf{Y}}_\mathbf{n}) = A\exp(f-f_0)^2\mathbf{S_n}\mathbf{S_n}^T \tag{35}$$

The peak frequency, f_0, was chosen at 1KHz where the ASD of each sensor is flat and the band-limited PCA was done in the frequency range (950,1050)Hz. This choice of frequency range has the effect of considering a 100Hz bandwidth injected noise source. The width of the gaussian in equation 35 is much narrower than 100Hz, but, as described in equation 32, it is only the integral of the gaussian over the (950,1050)Hz range that affects the PCA. Therefore it is convenient to choose a 1Hz width gaussian and adjust the amplitude, A, to control the total noise power, σ_n^2. The amplitude, A, was defined relative to the true noise in the sensors in this frequency region. Without injected noise, a band-limited PCA was done to calculate the eigenvalue of the first principal component, λ_1. This represents the dominant variance before the noise is injected. Then, $\mathbf{CSD}(\tilde{\mathbf{Y}}_\mathbf{n})$ was used alone to calculate a covariance matrix and perform a PCA only considering the injected noises. The eigenvalue of the first principal component (the rest are zero), λ_n, is a simple function of A. Thus A was varied to consider values of $\frac{\lambda_n}{\lambda_1}$ from 10^{-3} to 10^3. At logarithmically spaced steps in this interval of injected variances, 100 random choices for $\mathbf{S}_n$, pulled from a uniform distribution of normalized vectors, were considered. For each one, a band-limited PCA was done with

the noise injected into the real sensor data. If the injected noise is sufficiently dominant over the other noise sources, then the PCA will produce $\mathbf{U}^1 = \pm\mathbf{S}_n$. To quantify the extent to which this is true, the angle between $\mathbf{U}^1$ and $\mathbf{S}_n$ was calculated. Deviation angles over 90 degrees were mapped back to $[0, 90]$ by $\theta \to 180 - \theta$. For each value of $\frac{\lambda_n}{\lambda_1}$, the results were averaged over 100 random $\mathbf{S}_n$ and the standard deviations of these distributions were taken as error bars. The results are shown in figure 9.

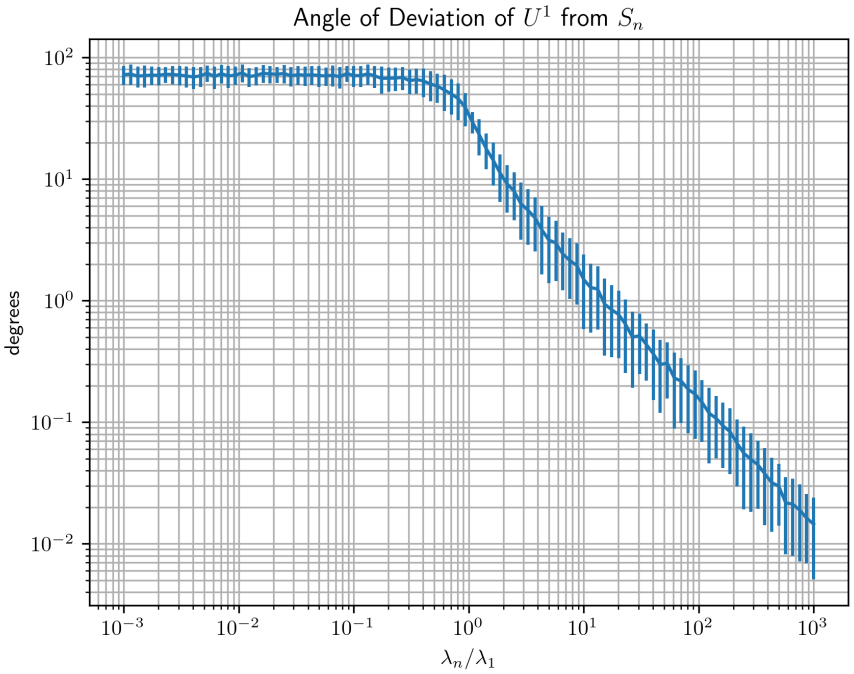

Figure 9: The deviation angles of $\mathbf{U}^1$ from $\mathbf{S}_n$ are calculated for 100 trials of random $\mathbf{S}_n$'s at values of $\frac{\lambda_n}{\lambda_1}$ ranging from 10^{-3} to 10^3.

Unsurprisingly, when the injected noise source is smaller or comparable to the dominant noise in the data, PCA does a poor job of extracting $\mathbf{S}_n$ from the data. When the injectected variance is larger, $\frac{\lambda_n}{\lambda_1} > 1$, the deviation angle decreases approximately $\propto \left(\frac{\lambda_n}{\lambda_1}\right)^{-1}$ signifying the improvement in the performance of the PCA. The results imply that a noise source with a variance 10x greater than other noises within a frequency range can yield band-limited PCA results with accuracy on the order of single degrees.

7.3 PCA of real noise spikes

This analysis technique was done on a $\sim$ 180 Hz feature in the PRCL calibrated dated. The PRCL calibrated sensor ASDs over the whole frequency range and zoomed in around the feature are shown in figure 10

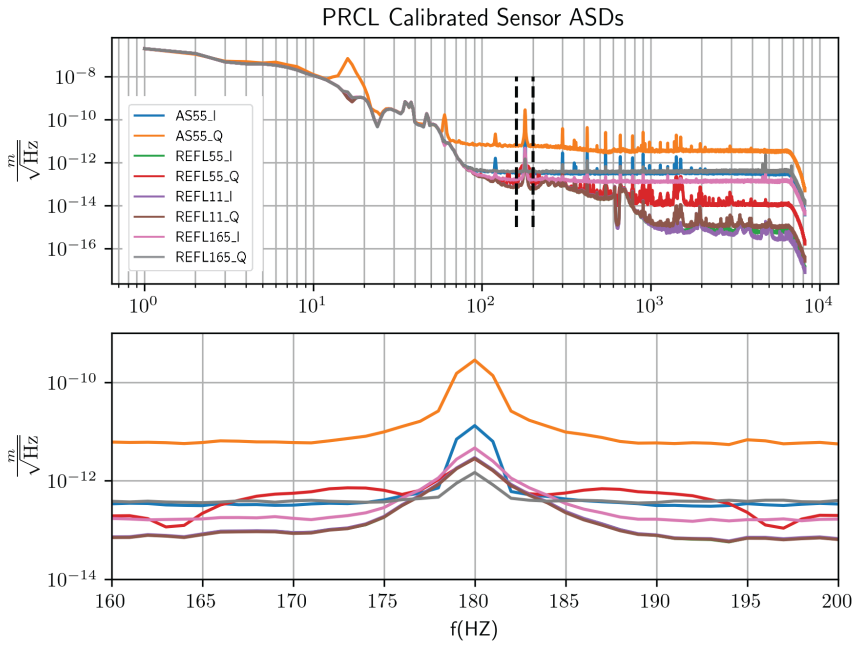

Figure 10: The ASD of the sensor data calibrated to PRCL and, in the lower figure, zoomed in around a $\sim$ 180 Hz feature.

The ASDs of the sensor linear combinations corresponding to the principal components, after the described renormalization, are displayed in figure 11. The result is largely consistent with expectations. The band-limited covariance matrix was calculated for the frequency range (175,185)Hz where the ASD of all the sensors contain this dominant feature. After transforming to the PCA basis, the first principal component presents the ASD with the largest noise spike about $\sim$ 100 times larger than the others. The second principal component also present a peak. The next several principal components don't present the peak feature, but at the expense of a larger ASD at other frequencies. The last two principal components show suppressed peaks at 180 Hz with the last one presenting $\sim$ 10 better SNR at 180Hz than any of the sensors.

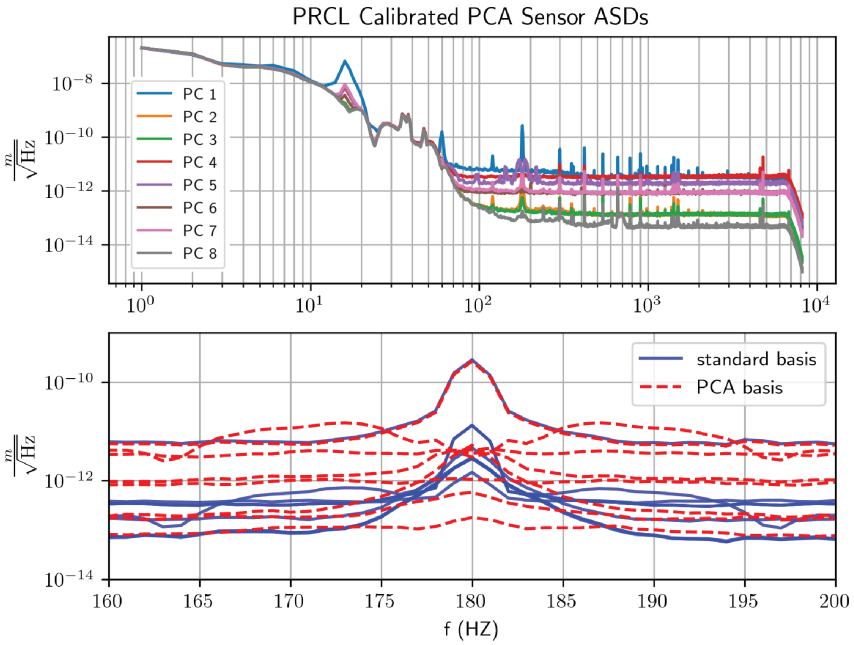

Figure 11: The ASD of the linear combinations, corresponding to the principal components, of sensor data calibrated to PRCL. The lower figure is zoomed in around a $\sim$ 180 Hz feature and plots the sensor data in blue and the principal component linear combinations in dashed red lines. One of the dashed red lines still presents the noise spike while the rest show a suppressed or no spike at all.

8 Summary and Next Steps

Methods have been developed to use measurements of the PRMI length sensing and control system to simulate the performance of the system with a new sensor fusion matrix $\mathbf{M}$ implemented. Two techniques for calculating $\mathbf{M}$ have been suggested and they are both predicted to reduce the amplitude spectral density of noise on both MICH and PRCL over a range of frequencies. These techniques should be evaluated on the 40m LIGO prototype by implementing the new sensor fusion techniques during a PRMI lock and measuring the resulting noise ASDs. In addition, new cost functions can be explored to optimize the $\mathbf{M}$ over different frequency ranges and with more sophisticated techniques to estimate the sensing noise.

In addition, the usefulness of principal components analysis to understand narrow frequency features in the sensors noise spectrum has been explored. The results suggest that band-limited PCA can extract information about the noise vector, $\mathbf{S}_n$ through which single dominant noise sources enter the space of sensor signals. Future work can explore the applications of this technique to the design of virtual sensors with improved SNR in narrow frequency regions or with frequency dependent sensor fusion to optimize SNR in several frequency ranges.

9 Acknowledgements

I'd like to thank Yehonathan Drori, Shruti Maliakal, Rana Adhikari and the other Caltech LIGO lab staff that helped me with this project. I am particularly grateful for Yehonathan's mentorship and the many hours of his time he dedicated to this project. In addition to these people, I owe thanks to the Caltech Summer Fellowship Program, LIGO, and the National Science Foundation for making this experience possible.

References

[1] B. P. Abbot et al. (LIGO Scientific Collaboration and Virgo Collaboration). Observation of Gravitational Waves from a Binary Black Hole Merger. Phys. Rev. Lett., 116, 061102 (2016).

[2] L. Sun et al. Characterization of systematic error in Advanced LIGO calibration. Class. Quantum Grav., 37, 225008 (2020).

[3] L. Barsotti, S. Gras, M. Evans, P. Fritschel. The updated Advanced LIGO design curve. (2018)

[4] LIGO Scientific Collaboration. Advanced LIGO. arXiv:1411.4547 (2014).

[5] E. A. Quintero et al. Improving the Performance and Sensitivity of Gravitational Wave Detectors. Review of Scientific Instruments, 87, 065107 (2016)

[6] Brett Shapiro. Intro to Control Theory for LIGO People. Lecture 2, G1600726-v3.